International Journal of Rock Mechanics & Mining Sciences 203 (2026) 106555

Contents lists available at ScienceDirect

International Journal of Rock Mechanics and Mining Sciences

journal homepage: www.elsevier.com/locate/ijrmms

Research Paper

Impact of pressure solution creep on the performance of salt caverns for underground hydrogen storage

Mohammad Saeed Amini [a,*], Hermínio T. Honório [b], Cornelis Vuik [a], Hadi Hajibeygi [b]

[a] Department of Applied Mathematics, Faculty of Electrical Engineering, Mathematics, and Computer Science, Delft University of Technology, Delft, The Netherlands
[b] Department of Geoscience and Engineering, Faculty of Civil Engineering and Geosciences, Delft University of Technology, Delft, The Netherlands

ARTICLE INFO

Keywords:
Underground hydrogen storage
Salt caverns
Pressure solution creep
Dislocation creep
Geomechanics
Numerical modeling

ABSTRACT

This study presents a numerical investigation of pressure solution creep and its influence on the mechanical behavior of salt caverns for underground hydrogen storage. A 3D modeling framework, implemented in the open-source simulator *SafeInCave*, incorporates both dislocation and pressure solution creep mechanisms and is applied to caverns with varying geometries, depths, temperatures, and interlayer positions under realistic conditions. The creep models are appropriately calibrated against experimental results from the literature to account for both stress and temperature effects. Results show that pressure solution creep becomes increasingly significant over time, particularly in shallow and cold formations, where it dominates deformation. It is more active away from cavern walls, where stresses and temperatures are low, while dislocation creep concentrates near the cavern walls and governs behavior at greater depths and higher temperatures. Overall, the study demonstrates that accurately capturing the effect of pressure solution creep is essential for reliable prediction of deformation and structural integrity in underground hydrogen storage caverns.

1. Introduction

The transition to renewable energy requires large-scale storage solutions to address the inherent intermittency of renewable energy generation.[1] Among various storage technologies, underground hydrogen storage (UHS) is one of the most promising one, due to hydrogen's high energy density and clean combustion properties.[2] With the potential to provide large-scale storage, UHS plays a critical role in stabilizing the power grid and enhancing the reliability of renewable energy systems.[3,4] However, ensuring safe and efficient large-scale hydrogen storage remains a key challenge in the energy transition, with geological formations offering the most viable and scalable solution.[5] Salt formations, including bedded salt deposits and salt domes, provide a geologically favorable environment for underground hydrogen storage. These formations, being widely distributed across many continents particularly Europe and Asia, are regularly assessed to evaluate their potential and storage viability.[6–8]

Salt caverns are crucial for underground hydrogen storage due to their extremely low permeability, high structural integrity, and self-healing properties, which facilitate repeated hydrogen injection and withdrawal.[5,9–11] However, their long-term stability under cyclic loading conditions remains a critical concern.[12,13] The processes of hydrogen injection and withdrawal induce time-dependent deformation mechanisms, potentially leading to cavern closure, permeability changes, and mechanical instability over extended periods of time.[14,15]

Accurate numerical modeling of stress and deformation of salt caverns is essential for evaluating their long-term performance under different operational conditions.[16] The cyclic pressurization and depressurization of these caverns introduce complex geomechanical responses, necessitating a comprehensive understanding of stress redistribution, deformation mechanisms, and time-dependent creep behavior.[17,18] These factors significantly influence the long-term structural integrity of salt caverns, being crucial for successful operations and abandonment.[19,20] Therefore, reliable simulation of these complex deformation mechanisms and investigating the stress intensities during underground hydrogen storage operations is crucial.[13,21]

The stability and long-term integrity of salt caverns subject to hydrogen storage conditions remains as an important topic in the literature.[13] The mechanical behavior of salt rock, particularly its creep response, plays a pivotal role in determining the durability and reliability of these caverns over extended periods.[22] As such, a comprehensive understanding of the underlying creep mechanisms is essential for ensuring the safe and sustainable storage of hydrogen.[23] An experimental–numerical study of salt cavern stability under cyclic loading was presented by Ref. 24, showing that cyclic pressurization

* Corresponding author.
E-mail address: mmohammadsaeed@tudelft.nl (M.S. Amini).

https://doi.org/10.1016/j.ijrmms.2026.106555
Received 6 November 2025; Received in revised form 6 April 2026; Accepted 23 April 2026
Available online 30 April 2026
1365-1609/© 2026 The Authors. Published by Elsevier Ltd. This is an open access article under the CC BY license (http://creativecommons.org/licenses/by/4.0/).

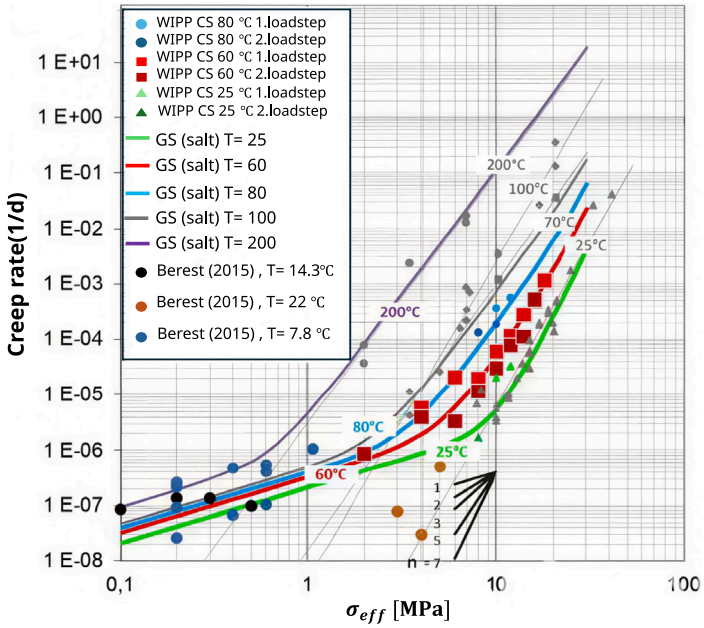

Fig. 1. Creep rate as a function of effective stress for various salt specimens under different temperature conditions (from Ref. 25.) Here, σ_{eff} represents the von Mises stress, and the creep rate is measured in units of per day.

strongly influences stress redistribution, cavern convergence, and long-term stability, while highlighting the importance of thermo-mechanical coupling and non-ideal cavern geometries in realistic performance assessment.

Salt rock deformation under stress is governed by three distinct creep phases: primary, secondary, and tertiary creep.[26,27] The primary creep involves rapid initial deformation driven by dislocation movement within the crystal lattice. This is followed by the secondary, or steady-state, phase in which the deformation occurs. Once the stress surpasses the dilatancy threshold, the tertiary creep initiates, resulting in accelerated deformation and eventually failure due excessive accumulation of damage.[27,28] The two principal mechanisms controlling steady-state in salt caverns are dislocation creep and pressure solution creep. Dislocation creep, which occurs dominant at higher stresses and temperature values due to lattice defects, has been extensively investigated through laboratory experiments to assess its impact on the long-term stability and structural integrity of underground storage systems.[29–34] In contrast, pressure solution is a stress-driven mechanism involving the dissolution of mineral grains at high-stress contact points and their subsequent reprecipitation in lower-stress regions, facilitating grain deformation at relatively low stresses in the presence of brine.[27,28,35] While both mechanisms have been studied in the context of rock mechanics, the growing application of salt caverns for underground hydrogen storage has resulted in increasing interests in understanding how the two creep mechanisms contribute to the overall response of the system, specially over many years of cyclic operations.[12,13,27,35–40]

A growing body of experimental, microstructural, and numerical evidence has demonstrated that pressure solution creep plays a decisive role in the time-dependent deformation of rock salt. Laboratory and field investigations have shown that dissolution precipitation processes along grain boundaries facilitate long-term strain accumulation and markedly influence cavern stability under operational conditions.[30,41–44] Recent modeling studies further emphasize that accurate representation of pressure solution mechanisms is essential for reproducing observed deformation rates and predicting the safe and efficient performance of hydrogen storage caverns.[22,23,25] Moreover, investigations addressing cyclic pressurization and depressurization demonstrate that pressure solution creep governs the mechanical response of salt caverns during repetitive loading, strongly affecting convergence, closure, and long-term integrity.[12,45] Collectively, these studies confirm that pressure solution creep is a governing mechanism that must be explicitly included in constitutive models to ensure reliable prediction of deformation in subsurface hydrogen storage systems.

As shown in Fig. 1, the dataset includes laboratory measurements from WIPP, BGR, and Bérest studies, covering a temperature range from 7.8 °C to 200 °C. The experimental results are fitted using the material constitutive law presented in Ref. 46. The figure reveals that creep rate is strongly dependent on temperature and a non-linear stress dependency (i.e., $n > 1$) is observed for higher stresses, which is attributed to dislocation creep mechanism. At lower stresses (< 5 MPa), however, creep rates present a linear dependency on stress, suggesting pressure solution mechanism is dominant over dislocation creep.[25] This is in accordance to microstructural analyses showing the important role of dissolution, diffusion, and precipitation in controlling deformation.[42]

A comprehensive review of geomechanical aspects of underground hydrogen storage (UHS) in both depleted reservoirs and salt caverns was presented by Ref. 47. Combining laboratory, numerical, and field-scale studies, the review emphasizes that cyclic hydrogen injection and withdrawal strongly influences stress redistribution and cavern deformation, underscoring the need for constitutive models capturing time-dependent mechanisms. In particular, recent investigations suggest that, although transient and reverse transient creep mechanisms are essential to fit cyclic triaxial tests, steady-state dislocation creep deformations (pressure solution was not included) plays a dominant role for field scale simulations.[48] Salt cavern simulations with constitutive models including pressure solution creep have been performed by many authors.[37,45,49–51] However, given the importance of pressure solution creep, a thorough understanding and systematic investigation of when and under which circumstances pressure solution creep is more or less important is still lacking. Moreover, model calibration has been shown to be both challenging and crucial for accurate results in salt cavern simulations.[16,48] To the best of authors knowledge, a systematic calibration procedure simultaneously performed for both dislocation and pressure solution creep have not been presented in the literature.

A range of constitutive formulations has been proposed to represent time-dependent deformation of rock salt. Many cavern-scale studies employ steady-state power-law (Norton-type) dislocation creep relations

or multi-mechanism formulations such as the Munson-Dawson model, which efficiently capture high-stress and high-temperature behavior but may underestimate deformation at low deviatoric stress levels.[52,53] Laboratory investigations have shown that pressure solution creep becomes increasingly important under low-stress conditions, where diffusion-controlled mechanisms dominate long-term deformation.[25,42] Recent cavern-scale studies under cyclic loading further highlight the sensitivity of stability and convergence to constitutive assumptions and operational pressure histories.[54] These developments indicate that model applicability strongly depends on the stress–temperature regime and loading path, motivating systematic comparison of creep mechanisms under hydrogen-relevant cyclic operation.

While numerous numerical studies have investigated salt cavern behavior during gas storage operations, most existing works primarily focus on dislocation creep or consider pressure solution effects in a limited or qualitative manner. The present study advances beyond prior approaches by systematically integrating pressure solution creep with dislocation creep within a calibration and by explicitly accounting for cyclic gas pressurization representative of underground hydrogen storage, together with constant-pressure reference cases. By quantifying their competing roles across varying temperatures, depths, cavern geometries, and interlayer configurations, this work provides a unified assessment of when and where pressure solution creep governs deformation. This systematic comparison enables improved prediction of cavern convergence and operational stability, thereby addressing a key gap in current cavern-scale geomechanical simulations. Although the intrinsic creep behavior of salt is independent of the stored gas type, underground hydrogen storage is characterized by more frequent cyclic pressure variations than conventional natural gas storage, which can amplify time-dependent deformation and cavern convergence.

In this context, the primary objective of this research is to quantify the influence of pressure solution creep on the stability of salt caverns used for cyclic hydrogen storage. More specifically, it is intended to identify under which operational conditions and salt cavern configurations pressure solution creep tends to be more or less important. The adopted three dimensional numerical modeling framework enables a systematic evaluation of how pressure solution creep affects the mechanical response of salt formations under low deviatoric stress conditions (below 5 MPa), where laboratory evidence indicates that diffusion controlled deformation dominates.[25,42] This analysis provides essential insight into the deformation mechanisms governing cavern integrity and their implications for the safe and efficient operation of underground hydrogen storage systems.

To achieve this analysis, a comprehensive deformation model (elastic, dislocation creep, and pressure solution creep mechanisms) is utilized with and without the pressure solution creep component. Additionally, a calibration procedure is presented for both dislocation and pressure solution creep models with respect with temperature and stress, such that the experimental results shown in Fig. 1 are reproduced. For various types of salt caverns, including complex geometries with interlayers at their top, middle and bottom, the influence of pressure solution creep is quantified over many cycles of operations. Results are investigated to highlight the influence of pressure solution, particularly after extended periods of operation. To validate the implementation of the pressure solution mechanism in our simulator, benchmarking with the lab data has been performed on block-shaped salt rock samples. All the implementations are made in the open-source SafeInCave simulator.[48]

While the constitutive creep formulations adopted in this study are established in the literature, the contribution of the present work lies in their calibration and systematic comparison under hydrogen-relevant cyclic loading. By integrating pressure solution creep with dislocation creep and quantifying their competing roles across temperature, depth, cavern geometry, and interlayer configurations, this study provides a focused cavern-scale assessment of long-term deformation mechanisms. Thermal effects are represented through prescribed temperature scenarios to isolate creep-driven mechanical behavior, while fully coupled thermo-hydro-mechanical evolution during leaching is beyond the scope of the present work.

While mathematical developments are not the primary focus of this study, we emphasize the underlying deformation physics by incorporating pressure solution creep into a fully implicit three-dimensional framework. Beyond routine sensitivity analyses, the simulations are designed to systematically isolate competing creep mechanisms and quantify their impact on cavern convergence, which has received limited attention in prior cavern-scale studies.

The rest of the manuscript is structured as follows. Next, the governing equations are presented, where the pressure solution mathematical model is presented along with other deformation mechanisms in great details. Then, in Methodology Section, simulation strategy and test cases description are presented. Cavern geometries, mesh topologies, material parameters etc. are all described in the Methodology Section. Next, Numerical results are presented in a following section. First, calibrations and validations against laboratory tests are presented, and then simulation results for various test cases under different loading conditions and configurations are presented. The paper is finally concluded with important remarks and learning points.

2. Governing equations

Salt rock deformation under a given load is time dependent and involves both elastic and inelastic mechanisms. For reliable assessment of the integrity of the caverns under cyclic loading, relevant to underground hydrogen storage, the constitutive models used to describe such complex deformations must include these mechanisms accurately.[55] Under equilibrium conditions, the principle mathematical formulation that governs momentum balance reads

$$\nabla \cdot \boldsymbol{\sigma} = \mathbf{f}, \tag{1}$$

where $\boldsymbol{\sigma}$ is the stress tensor and $\mathbf{f}$ denotes the body force per unit volume. Eq. (1) is subject to appropriate boundary and initial conditions, the appropriate consideration of which, beside the model construction and parameter calibration, also influences performance estimations and stability analyses.

To solve Eq. (1), one has to define a consistent relationship between the stress and strain (deformation) tensors, which is done via the choice of constitutive models, presented next.

2.1. Constitutive model

The constitutive model adopted in this work incorporates elastic and steady-state creep components, representing the primary mechanisms governing the mechanical behavior of rock salt under stress.[45] A conceptual representation of the constitutive model is depicted in Figs. 2 and 3(a). Additionally, the small-strain assumption is adopted such that the principle of additive decomposition can be applied. In this manner, the total strain can be written as

$$\boldsymbol{\varepsilon} = \boldsymbol{\varepsilon}_e + \boldsymbol{\varepsilon}_{ds} + \boldsymbol{\varepsilon}_{ps}, \tag{2}$$

where $\boldsymbol{\varepsilon}_e$ denotes the elastic strain. Moreover, $\boldsymbol{\varepsilon}_{ds}$ and $\boldsymbol{\varepsilon}_{ps}$ represent the strains associated with the dislocation and pressure solution creep responses, respectively.

The stress tensor relates to the elastic strain tensor according to Hooke's law, i.e.,

$$\boldsymbol{\sigma} = \mathbb{C} : \left(\boldsymbol{\varepsilon} - \boldsymbol{\varepsilon}_{ie}\right), \tag{3}$$

where the inelastic strain, in this case, is $\boldsymbol{\varepsilon}_{ie} = \boldsymbol{\varepsilon}_{ds} + \boldsymbol{\varepsilon}_{ps}$. Moreover, $\mathbb{C}$ represents the fourth-order elastic tensor, whose components are given by

$$C_{ijkl} = \lambda \delta_{ij}\delta_{kl} + \mu(\delta_{ik}\delta_{jl} + \delta_{il}\delta_{jk}), \tag{4}$$

where δ_{ij} denotes the Kronecker delta function, and λ and μ are the first and second Lamè's parameters.[56]

Next, the mathematical models for dislocation ($\boldsymbol{\varepsilon}_{ds}$) and pressure solution ($\boldsymbol{\varepsilon}_{ps}$) creep are presented.

Table 1
Summary of creep mechanisms considered in this study and their governing relations, stress dependence, and cavern-scale roles.

Creep mechanism	Governing form	Stress dependence	Cavern-scale role
Dislocation creep (ds)	$\dot{\varepsilon}_{ds} = A_{ds}\exp\left(-\frac{Q_{ds}}{RT}\right) q^{n-1} s$	Power-law	Dominates near the cavern wall under higher stress and elevated temperature, contributing to localized deformation and stress redistribution
Pressure solution creep (ps)	$\dot{\varepsilon}_{ps} = \frac{A_{ps}}{T d^m}\exp\left(-\frac{Q_{ps}}{RT}\right) s$	Linear	More relevant at lower stress and temperature, driving long-term bulk cavern convergence away from the cavern wall
Combined (ds+ps)	$\dot{\varepsilon}_{ie} = \dot{\varepsilon}_{ds} + \dot{\varepsilon}_{ps}$	Mixed	Interaction of near-wall deformation and long-term cavern closure

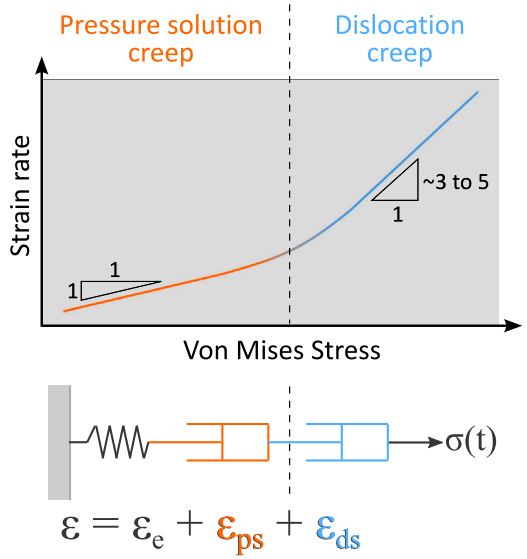

Fig. 2. Schematic illustration of strain rate as a function of von Mises stress, showing the transition from pressure solution creep (ε_{ps}) to dislocation creep (ε_{ds}). At low stress, the strain rate increases linearly with stress (slope ≈ 1), while at higher stress, dislocation creep dominates, following a power-law relation (stress exponent ≈ 3–5). The lower part shows a rheological model with elastic (ε_e), pressure solution, and dislocation creep.

2.1.1. Dislocation creep mechanism

Dislocation creep is a dominant deformation mechanism in salt rock under high deviatoric stress conditions and elevated temperatures. The dislocation creep mechanism is commonly described by a power-law function together with Arrhenius' law.[23] The expression for the dislocation creep strain rate can be written as

$$\dot{\boldsymbol{\varepsilon}}_{\mathrm{ds}} = A_{\mathrm{ds}} \exp\left(-\frac{Q_{\mathrm{ds}}}{RT}\right) q^{n-1}\mathbf{s}, \tag{5}$$

where $\mathbf{s}$ and q are the deviatoric and von Mises stress terms, respectively. Moreover, A_{ds} is a material parameter, n is the stress exponent, Q is the activation energy, R is the universal gas constant ($8.314\,\mathrm{J\ mol^{-1}\ K^{-1}}$), and T represents the absolute temperature.

2.1.2. Pressure solution creep mechanism

The pressure solution creep is a slow process controlled by diffusion in which mineral grains dissolve under high pressure and precipitate in regions of lower stress.[42] In the present framework, pressure solution creep is modeled as a diffusion-controlled micro-mechanical process involving stress-enhanced dissolution at grain contacts, mass transport through intergranular fluid films, and precipitation in pore spaces. This process can be mathematically described as

$$\dot{\boldsymbol{\varepsilon}}_{\mathrm{ps}} = \frac{A_{\mathrm{ps}}}{T d^m} \exp\left(-\frac{Q_{\mathrm{ps}}}{RT}\right)\mathbf{s}, \tag{6}$$

where d is the grain diameter, m is the grain size exponent and A_{ps} is a material parameter. Moreover, as in the dislocation creep equation, $\mathbf{s}$ denotes the deviatoric stress, Q is the activation energy, R is the universal gas constant ($8.314\,\mathrm{J\ mol^{-1}\ K^{-1}}$), and T represents the absolute temperature.

Deviatoric stress $\mathbf{s}$ plays a fundamental role in creep mechanisms as it governs inelastic deformation in materials,[57,58] and is defined as

$$s_{ij} = \sigma_{ij} - \frac{1}{3}\delta_{ij}\,\sigma_{kk}. \tag{7}$$

von Mises stress q plays an important role in determining the effective stress acting on the material during the creep process,[59,60] and is defined as

$$q = \sqrt{\frac{3}{2}\,\mathbf{s}_{ij}\mathbf{s}_{ji}}. \tag{8}$$

2.1.3. Complete constitutive model for salt rock creep

To accurately capture the time-dependent deformation behavior of salt rock under underground hydrogen storage conditions, a comprehensive rheological model is required. This model integrates the principal inelastic deformation mechanisms (dislocation and pressure solution creep) combined with an elastic element to represent recoverable strain. The total inelastic strain rate, i.e., $\dot{\boldsymbol{\varepsilon}}_{\mathrm{ie}}$, can thus be decomposed into contributions from dislocation creep $\dot{\boldsymbol{\varepsilon}}_{\mathrm{ds}}$ and pressure solution creep $\dot{\boldsymbol{\varepsilon}}_{\mathrm{ps}}$, i.e.,

$$\dot{\boldsymbol{\varepsilon}}_{\mathrm{ie}} = \dot{\boldsymbol{\varepsilon}}_{\mathrm{ds}} + \dot{\boldsymbol{\varepsilon}}_{\mathrm{ps}}. \tag{9}$$

The total inelastic strain rate is, therefore, given by

$$\dot{\boldsymbol{\varepsilon}}_{\mathrm{ie}} = A_{\mathrm{ds}} \exp\left(-\frac{Q_{\mathrm{ds}}}{RT}\right) q^{(n-1)}\mathbf{s} + \frac{A_{\mathrm{ps}}}{T} \exp\left(-\frac{Q_{\mathrm{ps}}}{RT}\right)\mathbf{s}. \tag{10}$$

Table 1 provides a concise overview of the dominant creep mechanisms considered in this study and their respective governing relations and cavern-scale implications.

Accordingly, the combined (ds+ps) and dislocation creep (ds) formulations are adopted to represent both near-wall deformation and long-term cavern convergence.

To isolate the influence of pressure solution creep on the overall deformation of the cavern, this study compares two constitutive models: (i) one considering elastic and dislocation creep responses, and (ii) another one incorporating elastic, dislocation and pressure solution creep responses. This comparative approach enables quantification of

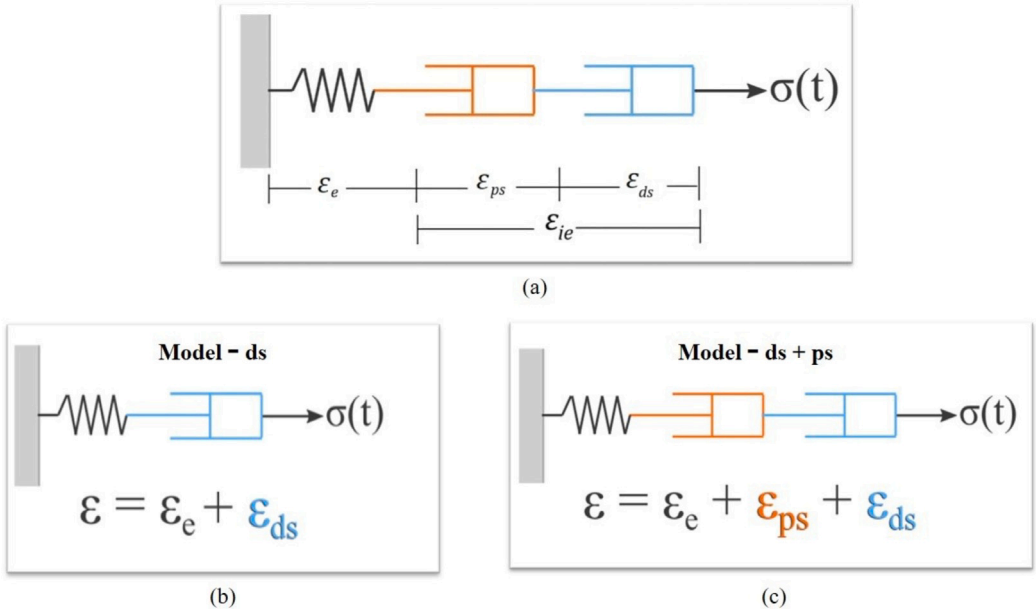

Fig. 3. (a) Elements composing the constitutive model, (b) Constitutive models (ds) is elastic and dislocation creep and (c) Model (ds+ps) is elastic, dislocation creep and pressure solution creep.

the pressure solution creep's contribution to both short- and long-term deformation, thereby clarifying its role in the mechanical deformation and stability of salt caverns. As illustrated in Fig. 2, the combined mechanical behavior of pressure solution and dislocation creep is shown as a function of von Mises stress. At low stress levels, strain rate is primarily governed by pressure solution creep, exhibiting a linear stress dependence. With increasing stress, dislocation creep becomes dominant, characterized by a nonlinear, power-law relationship with a typical exponent between 3 and 5. The rheological model depicted at the bottom of the figure captures this behavior using a spring and two dashpot elements in series, representing the total strain as the sum of elastic, pressure solution, and dislocation creep components.

3. Methodology

This section outlines the methodological framework adopted to investigate the mechanical behavior of salt caverns under conditions representative of underground hydrogen storage. The analysis begins with the formulation of the governing equations and constitutive models used to characterize both elastic deformation and creep mechanisms, with a particular emphasis on pressure solution creep. These constitutive formulations are implemented in the open-source, three-dimensional simulator *SafeInCave*,[c] which solves the geomechanical problem using a robust numerical scheme and simulation strategy.[48] Additional details of the numerical solution strategy, including the fully implicit time integration and Newton–Raphson linearization, are provided in Appendix A. The present study builds upon this validated numerical framework to focus on the calibrated integration of pressure solution creep with dislocation creep and their systematic cavern-scale comparison under hydrogen-relevant cyclic loading conditions.

To systematically evaluate the role of pressure solution creep in cavern evolution, a series of well-structured numerical test cases is presented. Each test scenario is developed to isolate and examine a specific facet of this mechanism under varying boundary and loading conditions. These simulations serve two primary objectives: (1) to facilitate model calibration against experimental or literature-based data, and (2) to quantify the influence of pressure solution creep on salt caverns.

3.1. Constitutive models

Fig. 3(b and c) illustrates the constitutive models used in this study. The Model (ds) comprises elastic and dislocation creep elements, while Model (ds+ps) incorporates elastic, dislocation creep, and pressure solution creep elements. The comparison between these models aims to assess the significance of pressure solution creep in influencing the mechanical behavior of salt rocks.

3.2. Simulation strategy

To ensure transparency and reproducibility, this section describes the complete simulation strategy for one time step, with particular focus on how the pressure solution creep is incorporated into both the outer-loop nonlinear Newton–Raphson loop and the inner-loop linear system.

The mathematical details of the tangent (Jacobian) operator are provided in Appendix A. At each time step, i.e., advancing from [t^n to t^{n+1}], the Newton–Raphson procedure iterates over index k index until the residual norm falls below a prescribed tolerance. More precisely, at iteration $k+1$, the momentum balance equation reads

$$\nabla \cdot \boldsymbol{\sigma}^{k+1} = \mathbf{f}, \tag{11}$$

where

$$\boldsymbol{\sigma}^{k+1} = \mathbb{C} : \left(\boldsymbol{\varepsilon}^{k+1} - \boldsymbol{\varepsilon}_{ie}^{k+1}\right), \tag{12}$$

and $\boldsymbol{\varepsilon}_{ie}^{k+1} = \boldsymbol{\varepsilon}_{ds}^{k+1} + \boldsymbol{\varepsilon}_{ps}^{k+1}$ is the total inelastic strain at the iteration index $k+1$. A backward Euler time integration is performed in a time interval Δt, resulting in the following expression for the inelastic strain, i.e.,

$$\boldsymbol{\varepsilon}_{ie}^{k+1} = \boldsymbol{\varepsilon}_{ie}^{n} + \Delta t\, \dot{\boldsymbol{\varepsilon}}_{ie}^{k+1}, \tag{13}$$

where the superscript n indicates that the corresponding variable is evaluated at the known last time state t^n, while the superscript $k+1$ indicates the new iteration index to reach the current time t^{n+1}. Additionally, $\dot{\boldsymbol{\varepsilon}}_{ds}^{k+1}$ and $\dot{\boldsymbol{\varepsilon}}_{ps}^{k+1}$, constituting the total inelastic strain $\dot{\boldsymbol{\varepsilon}}_{ie}^{k+1}$, which depend on the stress $\boldsymbol{\sigma}^{k+1}$ (see Eqs. (5) and (6)).

[c] https://gitlab.tudelft.nl/ADMIRE_Public/safeincave

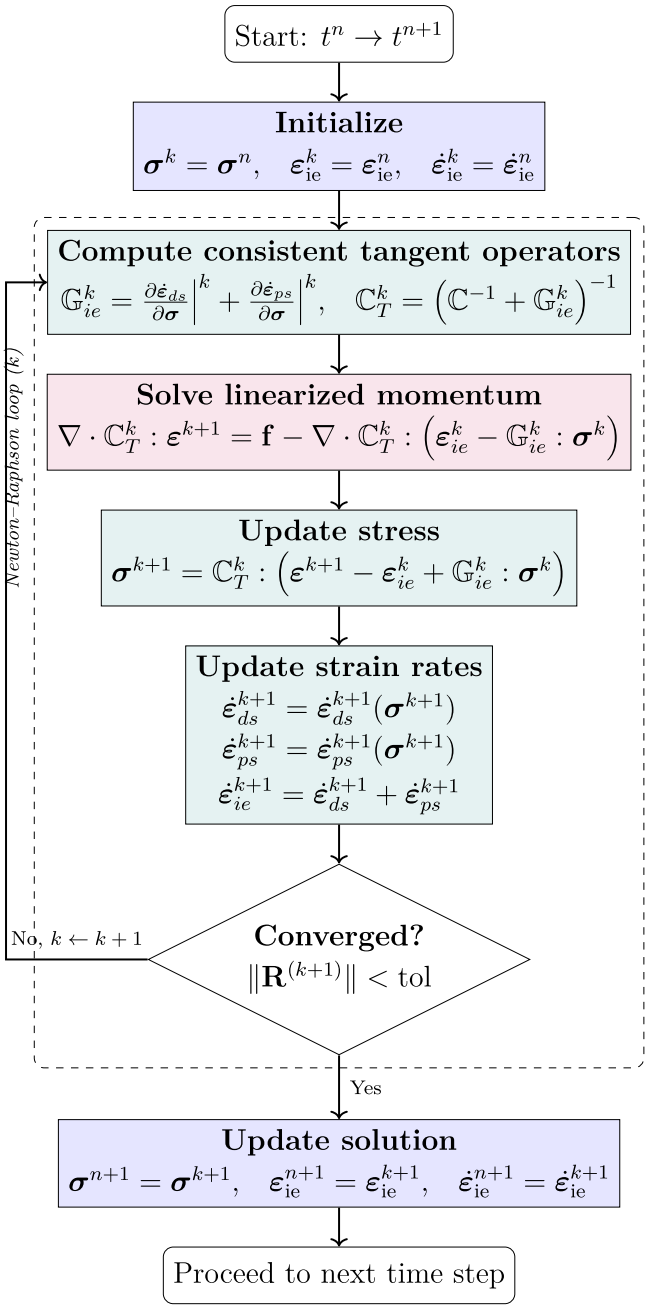

Fig. 4. Flowchart of the fully implicit Newton–Raphson iterations for one time step in *SafeInCave*, including dislocation and pressure solution creep.

The inelastic strain rate $\boldsymbol{\sigma}^{k+1}$ in Eq. (13) is linearized,[48] i.e.,

$$\dot{\boldsymbol{\varepsilon}}_{ie}^{k+1} = \dot{\boldsymbol{\varepsilon}}_{ie}^{k} + \mathbb{G}_{ie}^{k} : \delta\boldsymbol{\sigma}^{k+1}, \tag{14}$$

where $\delta\boldsymbol{\sigma}^{k+1} = \boldsymbol{\sigma}^{k+1} - \boldsymbol{\sigma}^{k}$ is the stress increment within the Newton–Raphson loop, and the Jacobian matrix $\mathbb{G}$ is calculated numerically and can be expressed as

$$\mathbb{G}_{ie}^{k} = \frac{\partial \dot{\boldsymbol{\varepsilon}}_{ie}^{k}}{\partial \boldsymbol{\sigma}} = \frac{\partial \dot{\boldsymbol{\varepsilon}}_{ds}^{k}}{\partial \boldsymbol{\sigma}} + \frac{\partial \dot{\boldsymbol{\varepsilon}}_{ps}^{k}}{\partial \boldsymbol{\sigma}}. \tag{15}$$

In this manner, combining Eqs. (14), (13) and (12) and solving for $\boldsymbol{\sigma}^{k+1}$ yields

$$\boldsymbol{\sigma}^{k+1} = \mathbb{C}_T^k : \left(\boldsymbol{\varepsilon}^{k+1} - \boldsymbol{\varepsilon}_{ie}^k + \mathbb{G}_{ie}^k : \boldsymbol{\sigma}^k\right), \tag{16}$$

where $\mathbb{C}_T^k = \left(\mathbb{C}^{-1} + \mathbb{G}_{ie}^k\right)^{-1}$ is the consistent tangent stiffness tensor.

Finally, substitution of Eq. (16) into Eq. (11) leads to the linearized momentum balance equation solved in SafeInCave, that is,

$$\nabla \cdot \mathbb{C}_T^k : \boldsymbol{\varepsilon}^{k+1} = \mathbf{f} - \nabla \cdot \mathbb{C}_T^k : \left(\boldsymbol{\varepsilon}_{ie}^k - \mathbb{G}_{ie}^k : \boldsymbol{\sigma}^k\right). \tag{17}$$

Here, $\boldsymbol{\varepsilon} = \frac{1}{2}\left(\nabla\mathbf{u} + \nabla\mathbf{u}^T\right)$ holds for infinitesimal strains, and $\mathbf{u}$ denotes the displacement vector.

Eq. (17) results in the linear system solved at each Newton–Raphson iteration. The Jacobian matrix of the linearized system depends explicitly on $\partial\dot{\varepsilon}_{ie}/\partial\sigma$, which includes the contribution of pressure solution creep through $\partial\dot{\varepsilon}_{ps}/\partial\sigma$. This derivative is stress-independent (see Appendix A, Eq. (21) for more information) but must be included at every iteration to preserve the quadratic convergence of the solver.

The numerical procedure for a single time step follows a fully implicit Newton–Raphson framework in which the coupled effects of dislocation and pressure solution creep are consistently incorporated. This is illustrated in the flowchart of Fig. 4, where the iterative cycle

begins by calculating the consistent tangent operators ($\mathbb{G}_{ie}$ and $\mathbb{C}_T$), followed by the solution of the linearized momentum equation, which provides displacements to calculate ϵ^{k+1}. This new total strain is used to update the stress field, which in turn is used to update the dislocation and pressure solution strain rates. This process is repeated until a convergence criterion is satisfied, before moving to the next time step.

3.3. Cavern geometries

This study employs an axisymmetric salt cavern geometry, generated using Gmsh, to represent realistic underground storage conditions. Three test cases are developed to assess the influence of key mechanical and geological parameters.

3.3.1. Test case 1

To ensure the accuracy and reliability of the numerical framework, a preliminary calibration and verification model was developed using a simplified cubic domain representing a homogeneous salt rock specimen. The model comprises a 1 m×1 m×1 m cube subjected to boundary and loading conditions consistent with laboratory-scale mechanical tests. Simulations were conducted at three distinct temperatures 25 °C, 60 °C, and 80 °C to investigate the temperature dependence of creep behavior (three constant temperature conditions maintained constant throughout the domain). Each model was subjected to a constant von Mises equivalent stress, denoted as q, ranging from 0.1 MPa to 100 MPa, to capture the transition in dominant creep mechanisms.

3.3.2. Test case 2

This geomechanical modeling scenario investigates the combined influence of cavern geometry (regular and irregular) and positioning of a distinct Carnallite interlayer. All simulations are conducted within a consistent three-dimensional domain of 2000 m×2000 m×1700 m. The stratigraphic model features a weak Carnallite interlayer (45 m) embedded between halite formations beneath a sedimentary overburden (400 m). By varying its position (top, middle, or bottom of the cavern), the study evaluates its impact on stress localization and deformation behavior. A total of 18 simulation models are developed that encompass two cavern geometries (regular and irregular), three positions between layers, and three temperature conditions maintained constant throughout the domain (25 °C, 60 °C, and 80 °C), to comprehensively investigate the combined effects of geometry, interlayer, and temperature on cavern behavior. In this test case, two operational scenarios were examined: (i) constant gas pressure to evaluate the displacement response (15 MPa) and (ii) cyclic gas pressure to analyze its impact on cavern convergence (10 MPa and 15 MPa). The irregular cavern geometries with various interlayer positions (top, middle, and bottom) used in this study are illustrated in Fig. 5(A). Details of the regular cavern geometry, are presented in the Supplementary Information (See Figure S1).

3.3.3. Test case 3

To assess the effects of cavern depth and geothermal gradients on mechanical behavior, a third series of models is developed by varying only the vertical position of an irregular cavern with constant geometry within a 2200 m × 2200 m × 2000 m domain. The models include a 400 m thick overburden and a 1600 m halite layer, with cavern placements at depths of 750 m, 1000 m, and 1300 m. A geothermal gradient of 27 °C/km is applied, starting at 25 °C at the surface and increasing linearly with depth throughout the domain. In this test case, the time-dependent cavern convergence was investigated under cyclic gas pressure conditions. The irregular cavern geometries, along with three different cavern positions considered in this study, are illustrated in Fig. 5(B).

3.4. Boundary and initial conditions

In Test Cases 2 and 3, displacement boundary conditions are applied to simulate a confined geological environment. All four vertical boundaries are fixed to prevent normal displacement, while the top surface remains free to allow the application of overburden stress and cavern pressure. An internal pressure is applied directly to the cavern wall under two scenarios (Test Cases 2): (1) a cyclic pressure fluctuating between 10 MPa and 15 MPa, and (2) a constant pressure of 15 MPa, used to isolate the influence of pressure solution creep. The domain is defined with impermeable boundaries and realistic vertical stress distributions based on material densities: 2000 kg/m^3 for the overburden, 2200 kg/m^3 for halite, and 1600 kg/m^3 for the Carnallite interlayer. Prior to the operational phase, an equilibrium preloading stage is performed to establish a realistic in-situ stress field based on gravity loading and imposed boundary constraints.

The initial in-situ stress state is established under lithostatic loading together with an initial uniform cavern pressure, prior to applying cyclic pressure schedules. The cavern geometry is assumed to be the outcome of the solution-mining process and is treated as a fixed initial void at $t = 0$. The initial condition is established by solving a mechanical equilibrium problem before applying any pressure schedule. During this preloading stage, a constant internal pressure of $p(t = 0) = 15$ MPa is applied uniformly to the cavern wall. The boundary conditions and gas pressure conditions for (Test Cases 2) the simulations are illustrated in Fig. 6. In test case 3, the cavern pressure during cyclic loading ranges between 80% (maximum) and 20% (minimum) of the lithostatic pressure. This setup enables direct comparison of depth-dependent stress distribution and deformation under consistent boundary and material conditions. In this study, “short-term” and “long-term” refer to the early (approximately 100 days) and later (approximately 300 days) stages of the simulated operational period, respectively.

3.5. Material parameters

The material parameters used in this study are categorized into three groups: elastic, dislocation creep, and pressure solution creep parameters. Elastic parameters, including Young’s modulus and Poisson’s ratio, are based on values from Ingraham et al.[61] The material parameters for dislocation creep and pressure solution creep for halite were extracted from our calibration results, whereas the corresponding parameters for carnallite were partially adopted from the literature.[25,45,62] Carnallite is adopted as a representative weak evaporite interlayer to assess the mechanical influence of low-stiffness layers on cavern stability, supported by experimental studies demonstrating its reduced strength and distinct creep behavior relative to halite.[62–64] Table 2 presents the complete set of material parameters, including those used for halite, the carnallite interlayer, and supporting materials, thereby enabling the implementation of the proposed constitutive model.

3.6. Code implementation

A Python-based three-dimensional finite element simulator has been developed to perform time-dependent geomechanical analyses. The formulation is implemented using the Dolfin interface,[65] part of the FEniCS Project version 2019.1.[66] Geometries and meshes are generated in Gmsh version 4.10.1,[67] and subsequently converted to the required .xml format using the dolfin-convert utility. The framework supports multiple time integration schemes, including explicit, Crank–Nicolson, and fully implicit methods. Iterative solvers with appropriate preconditioners are employed to ensure numerical efficiency. Its modular design enables straightforward integration of additional material models and boundary conditions. All simulations are performed on a standard workstation, with model calibration supported by automated parameter sweeps. The resulting open-source three-dimensional simulator, SafeInCave, is specifically designed to solve the non-linear governing equations governing salt cavern deformation.

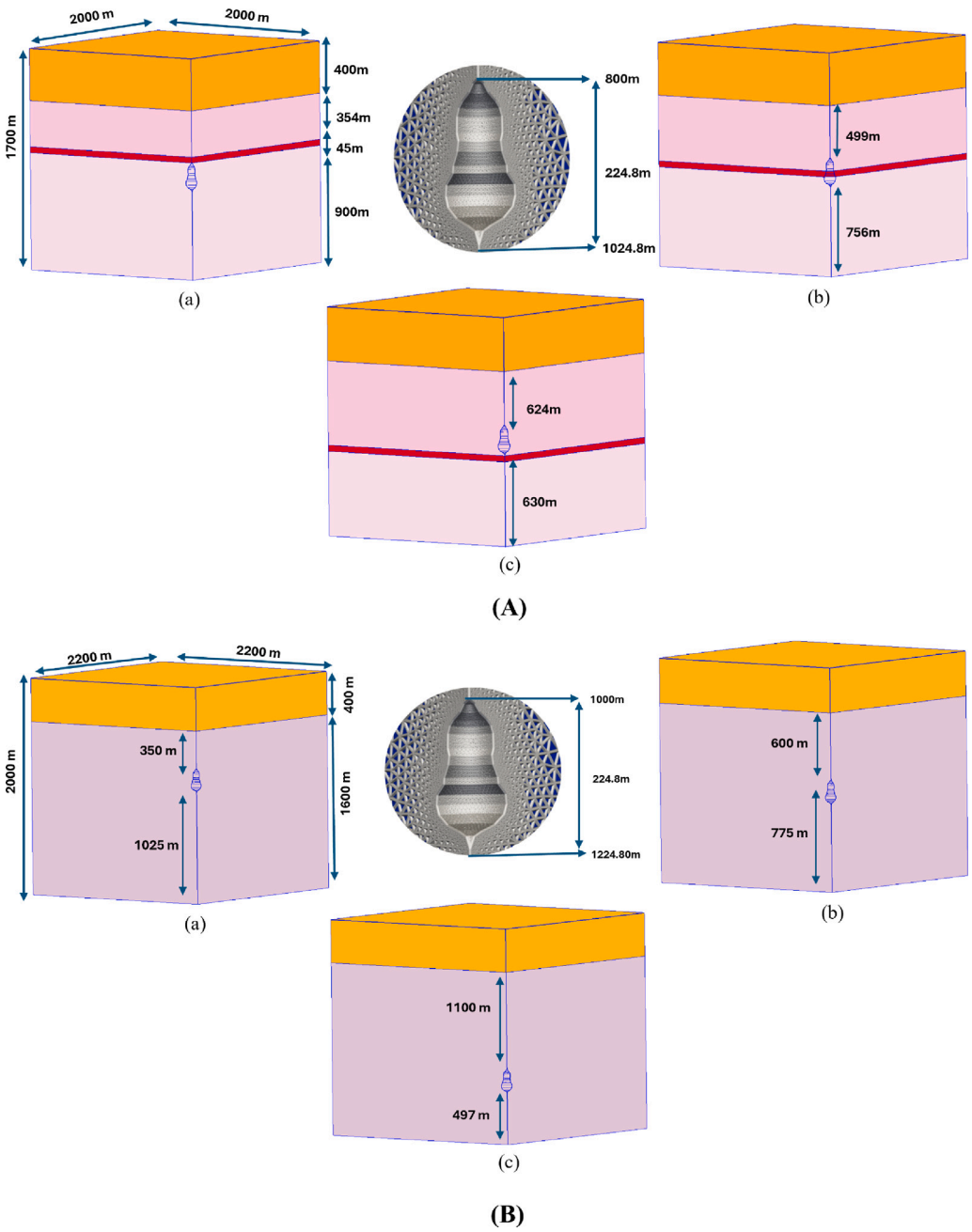

Fig. 5. (A) The irregular cavern model includes three interlayer positions: (a) top, (b) middle, and (c) bottom of the cavern. (B) Three different irregular cavern positions: (a) at a shallow depth, (b) at an average depth, and (c) at a great depth.

3.7. Model assumptions

The numerical models are constructed under simplifying assumptions to balance computational efficiency with geomechanical accuracy. Salt is modeled as a homogeneous, isotropic material with distinct constitutive laws for dislocation and pressure solution creep. A prescribed temperature gradient represents thermal effects, but heat transfer is not modeled. Temperature effects are incorporated through prescribed thermal conditions (constant temperatures or a geothermal gradient), while fully coupled thermo-mechanical evolution during leaching, including transient heat transfer and staged excavation, is beyond the scope of the present study. In this study, "cold" salt caverns refer to caverns with initial temperatures in the range of 20–30 °C, representative of shallow storage depths or low geothermal gradients, whereas "warm" caverns correspond to higher initial temperatures in the range of 60–80 °C, representative of deeper formations (Test Case 1 and 2). In addition a depth-dependent thermal profile is considered using a geothermal gradient of 27 °C/km, with the initial cavern temperature defined consistently with the corresponding storage depth (Test Case 3). Material properties are time-invariant, with no consideration of damage, fracturing, or chemical processes. These assumptions enable focused analysis of geometric, temperature, and mechanical influences on long-term salt cavern deformation. To account for geometric uncertainty arising from solution mining, both regular and irregular cavern geometries with varying interlayer positions are considered.

4. Numerical investigations and results

This section presents the results of the numerical simulations performed using the custom-developed finite element framework, namely the simulator SafeInCave.

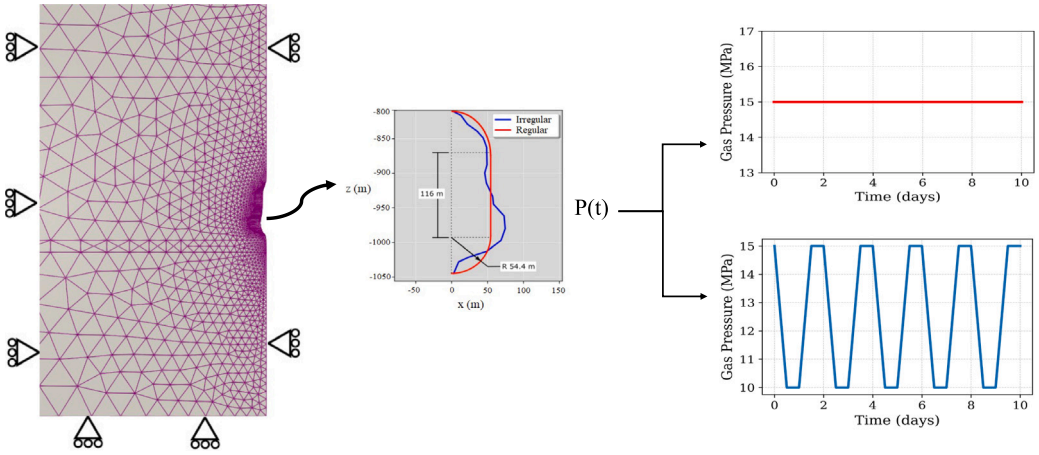

Fig. 6. Boundary conditions and pressure schedules for constant pressure (top-right) and cyclic loading (bottom-right) scenarios. (for Test Case 2).

Table 2
Sets of material properties for halite (Test Cases 1–3), carnallite interlayer (Test Case 2), and overburden.

Element	Halite	Carnallite	Overburden
Elastic			
E (GPa)	35	17	15
ν (–)	0.25	0.33	0.20
Dislocation creep			
A_{ds} ($Pa^{-n}s^{-1}$)	5.27×10^{-21}	2.75×10^{-30}	–
Q_{ds} (J/mol)	72 819	85 348	–
R (J K^{-1} mol^{-1})	8.32	8.32	–
n (–)	3.20	5.10	–
Pressure solution creep			
A_{ps} ($Pa^{-1}s^{-1}$)	1.29×10^{-19}	3.18×10^{-19}	–
Q_{ps} (J/mol)	13 184	32 526	–
R (J K^{-1} mol^{-1})	8.32	8.32	–
m (–)	3	3	–
d (mm)	10	10	–

Table 3
Material parameters extracted from the fitted curves based on Bérest et al. (2019).[25]

T, °C	$\bar{A}_{ds}(T)$	n	$\bar{A}_{ps}(T)$
25	3.00×10^{-33}	3.2	2.30×10^{-18}
60	2.00×10^{-32}	3.2	3.00×10^{-18}
80	9.00×10^{-32}	3.2	4.30×10^{-18}

4.1. Test case 1: Model calibration

The goal of this section is to calibrate the coefficients A_{ds}, Q_{ds}, n, A_{ps}, and Q_{ps} so that Eq. (10) reproduces the creep rate curves presented in Ref. 25 for 25 °C, 60 °C, and 80 °C. The procedure starts by performing individual calibrations for the creep curves for each temperature. Let us define the following functions:

$$\bar{A}_{ds}(T) = A_{ds} \exp\left(-\frac{Q_{ds}}{RT}\right) \quad \text{and} \quad \bar{A}_{ps}(T) = \frac{A_{ps}}{T} \exp\left(-\frac{Q_{ds}}{RT}\right). \tag{18}$$

We first find the values of n and the values of functions $\bar{A}_{ds}(T)$ and $\bar{A}_{ps}(T)$ that fit the creep curves corresponding to each temperature individually. The obtained values are shown in Table 3, and are also plotted in Fig. 7(a) and 7(b). The solid lines in Fig. 7(c) represent the individual creep curves obtained with the coefficients shown Table 3. The reason the fitted curve for $T = 25$ °C does not fit well with the experimental data is due to the choice of n, probably because a different salt was used for this experiment.

Based on the values of $\bar{A}_{ds}(T)$ presented in Table 4 and Figs. 7a, we use least-squares to find coefficients A_{ds} and Q_{ds} that better fit the

Table 4
Material parameters for use in analytical and numerical analyses.

T (°C)	A_{ds} ($Pa^{-n}s^{-1}$)	n (–)	Q_{ds} (J/mol)	A_{ps} ($Pa^{-1}s^{-1}$)	Q_{ps} (J/mol)
25, 60, 80	5.27×10^{-21}	3.2	72 820	1.29×10^{-13}	13 184

points. The same procedure is performed for obtaining the pressure solution coefficients. The obtained coefficients are summarized in Table 4, and the resulting curves for $\bar{A}_{ds}(T)$ and $\bar{A}_{ps}(T)$ are shown by the solid lines Fig. 7(a) and 7(b), respectively. The dashed lines in Fig. 7(c) are the creep curves obtained with Eq. (10) and the coefficients shown in Table 4. It can be verified that, except for dislocation creep rates at 25 °C, our creep model agrees well with the experimental data.

To verify the numerical implementation of the model, 30 simulations (cubic block of salt rock) were performed under various von Mises stress conditions at 25 °C, 60 °C, and 80 °C. Fig. 7(d) compares simulation results (colored markers), experimental (Bérest et al. 2019) (solid lines) and analytical results (dashed lines) obtained with Eq. (10). The agreement among the results across all temperatures confirms the accuracy and correct implementation of the numerical framework.

4.1.1. Comparison of dislocation and pressure solution creep coefficients

Fig. 8 compares the coefficients multiplying the deviatoric stress tensor (s) in the strain rate formulations for dislocation creep ($\bar{A}_{ds}(T,q)$) and pressure solution creep ($\bar{A}_{ps}(T)$), calculated using the same material parameters shown in Table 4. The results show that the relative importance of dislocation creep depends strongly on both temperature and von Mises stress, whereas pressure solution creep depends only on temperature. At low temperatures ($T \approx 25$ °C), $\bar{A}_{ps}$ is significantly larger than $\bar{A}_{ds}$ ($\bar{A}_{ps} \gg \bar{A}_{ds}$) for all stresses ($1 \le q \le 20$ MPa), indicating that pressure solution creep dominates in colder cavern conditions. At intermediate temperatures ($T \approx 60$ °C), pressure solution remains dominant only under low stresses ($q \lesssim 3$ MPa), whereas dislocation creep prevails at higher stresses. At high temperatures ($T \gtrsim 80$ °C), $\bar{A}_{ds}$ consistently exceeds $\bar{A}_{ps}$, confirming that pressure solution creep becomes negligible in deep, high-temperature salt formations.

Overall, this figure demonstrates that pressure solution creep is most significant at lower temperatures ($T < 40$ °C), while at higher temperatures ($T > 80$ °C) dislocation creep dominates regardless of stress. For example, at $T = 25$ °C and $q = 3$ MPa, $\bar{A}_{ps}$ is several times larger than $\bar{A}_{ds}$, whereas at $T = 80$ °C and the same stress level, $\bar{A}_{ds}$ surpasses $\bar{A}_{ps}$ by more than an order of magnitude. These trends highlight the importance of accurately considering pressure solution creep in long-term displacement modeling of shallow or colder salt formations, while it can often be neglected for deep, high-temperature

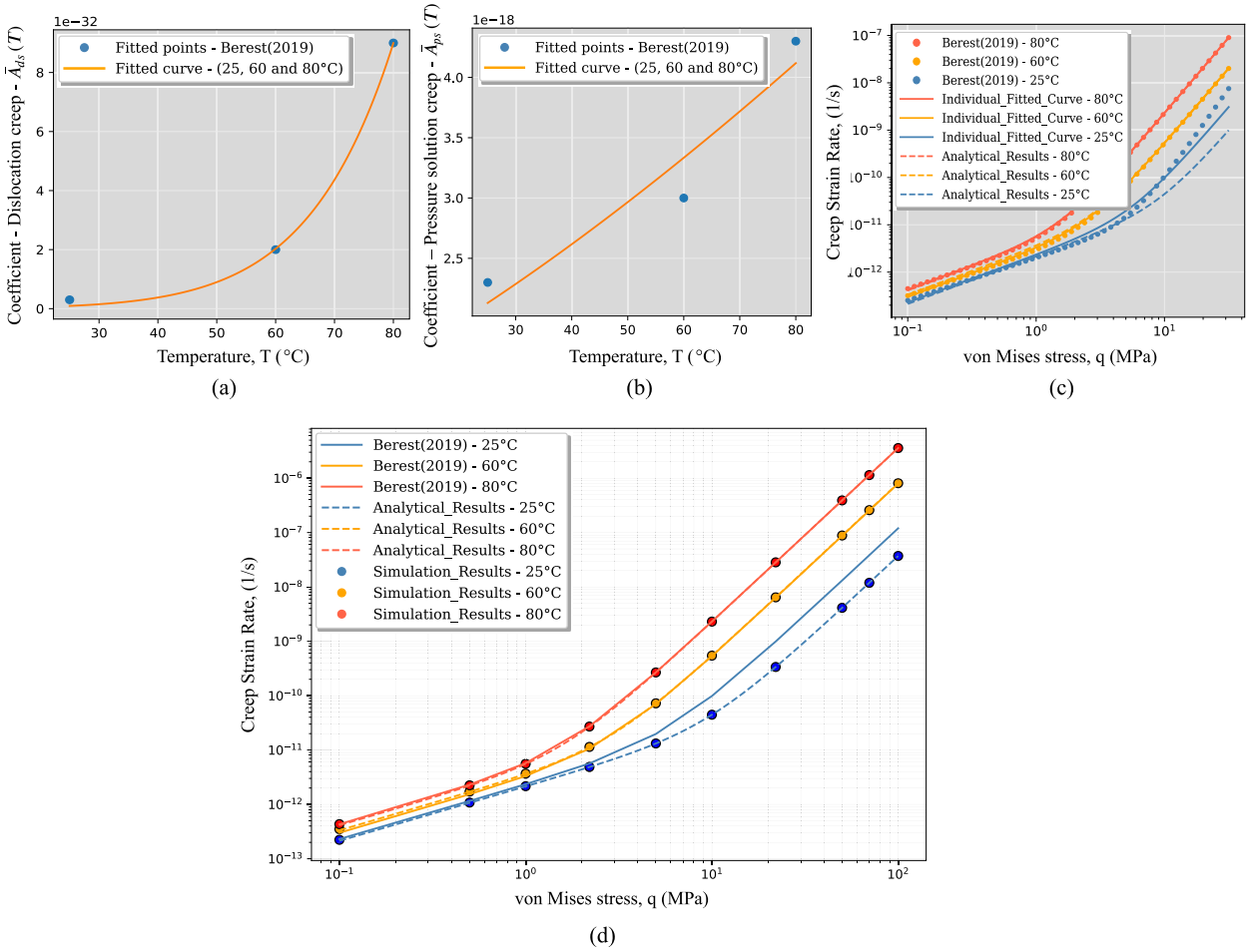

Fig. 7. Calibration and verification of the creep constitutive models. (a) Fitted curves for the temperature dependence of the dislocation creep coefficient $\bar{A}_{\mathrm{ds}}(T)$, with material parameters extracted from the fitted curves based on Bérest et al. (2019); (b) Fitted curves for the temperature dependence of the pressure solution creep coefficient $\bar{A}_{\mathrm{ps}}(T)$ based on Bérest et al. (2019); (c) Comparison between experimental data (Bérest et al. 2019), analytical results, and individual fitted curves; (d) Numerical simulation results compared with experimental (Bérest et al. 2019) and analytical results for 30 models at three temperatures.

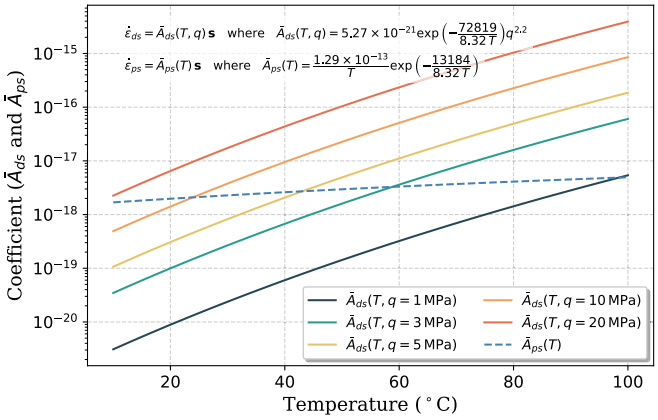

Fig. 8. Comparison of the temperature dependence of the dislocation creep coefficient ($\bar{A}_{ds}(T,q)$) and the pressure solution creep coefficient ($\bar{A}_{ps}(T)$) for various von Mises stresses ($q = 1, 3, 5, 10, 20$ MPa).

storage caverns. Notably, the effect of pressure solution creep is more pronounced at locations far from the cavern wall, where the von Mises stress is lowest, whereas dislocation creep dominates in regions closer to the cavern boundary, where von Mises stresses are higher.

4.2. Test case 2(a): Regular and irregular caverns with interlayer

All results in these cases present the time-dependent displacement at three points (A, B, and C) located adjacent to a irregular cavern with

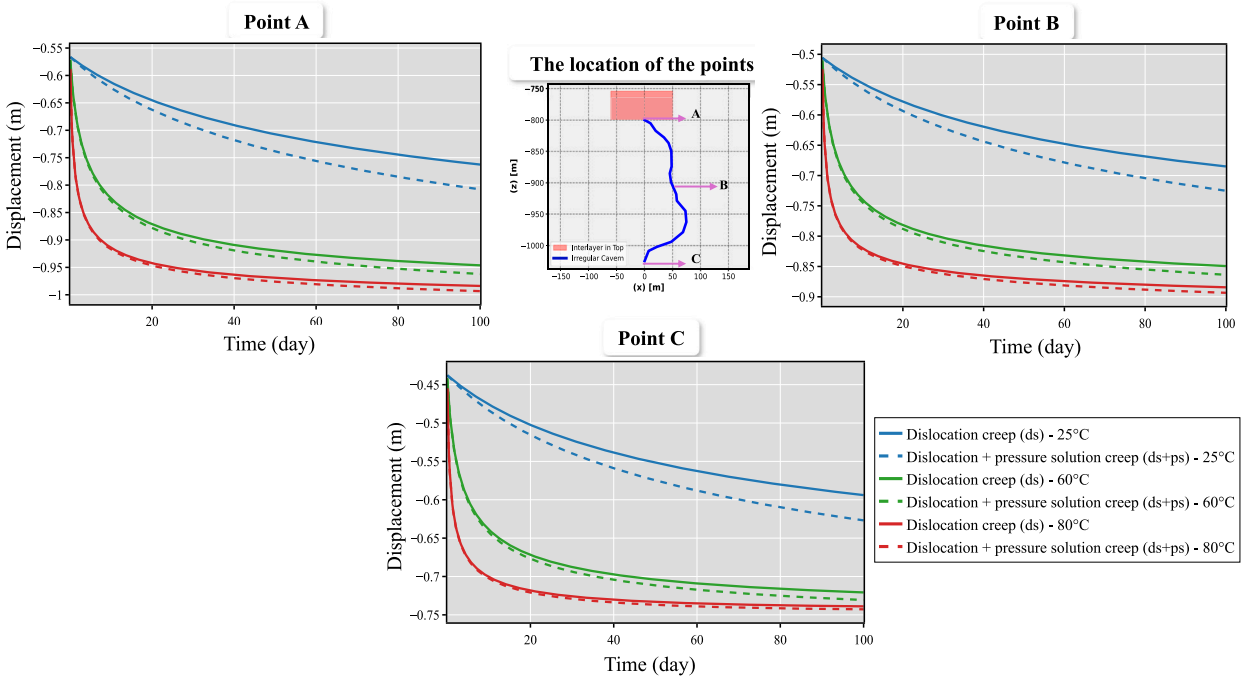

Fig. 9. Displacement at monitoring points A, B, and C for the irregular cavern geometry, with the carnallite interlayer located at the top of the cavern.

an interlayer (Carnallite) positioned at the top, middle and bottom of the model (thickness = 45 m). The analysis compares results for three temperature conditions (25 °C, 60 °C, and 80 °C) and for two creep scenarios: dislocation creep only (ds) and dislocation plus pressure solution creep (ds + ps), under constant gas pressure. Fig. 9 presents the displacement behavior at three points for the irregular cavern with the interlayer positioned at the top of the cavern. Point A, located near the top of the cavern and within the interlayer zone, exhibits the highest displacement among the three points. Also, the maximum displacement occurs at 80 °C. Point B, situated along the cavern wall, shows moderate displacement, while Point C, located at the bottom of the cavern, exhibits the lowest displacement.

Fig. 10(a) and 10(b) indicate that the highest displacement occurs at 80 °C. Additionally, the effect of pressure solution creep is more pronounced in the colder cavern compared to the warmer one.

Fig. 11 presents the evolution of displacement differences (Δu) between dislocation-only (ds) and dislocation plus pressure solution (ds + ps) creep for three interlayer positions (top, middle, and bottom of the irregular cavern) at 25 °C. In the top interlayer, Point B shows the highest displacement difference, reaching about 0.037 m after 300 days, whereas Point A remains slightly lower (0.030 m). The middle interlayer exhibits more significant displacement, with Point B increasing to approximately 0.044 m at 300 days, indicating enhanced creep activity in stress-concentrated regions. The bottom interlayer displays the strongest influence of pressure solution creep, with Point C attaining the highest displacement difference overall (around 0.055 m at 300 days). Conversely, Point A in the bottom interlayer records the lowest difference (roughly 0.017 m), consistent with its position farther from the most deformable zone. These results highlight the strong sensitivity of pressure solution creep to interlayer position and cavern geometry.

All results for the regular cavern are provided in the Supplementary Information (See Figures S2–S4), including displacement plots for points A, B, and C and the graphs for (Δu) and (See Figure S5).

4.3. Test case 2(b): Convergence behavior in regular and irregular caverns with interlayer effects

Fig. 12 shows a relationship between temperature and the magnitude of convergence under cyclic loading condition for regular (top) and irregular (bottom) caverns. Convergence, expressed as a percentage reduction from the initial volume, reflects the extent of time-dependent cavern wall displacement. Convergence increases with temperature, with the 80 °C condition showing the largest convergence cycles across all cases. The percentage difference between the dashed and solid lines at the end of 100 days illustrates that the difference is greatest at 25 °C. This suggests that pressure solution creep is more pronounced in the colder cavern (lower temperatures), contributing more significantly to total cavern convergence under cyclic loading. This finding is also observed under constant gas pressure conditions, where the results are similar to those obtained under cyclic loading. There is a slight difference between the regular and irregular caverns in the final values of convergence, indicating that the irregular cavern exhibits a higher convergence compared to the regular one. Additionally, when an interlayer is located in the middle of the cavern (thus directly influencing the cavern shape) the overall convergence is largest for both cavern geometries.

4.4. Test case 3: Irregular caverns at different depths

To evaluate the impact of pressure solution creep and cavern depth on volumetric closure, convergence was analyzed over time for shallow (blue), average (green), and great (red) depth cavern positions using dislocation (ds) and dislocation plus pressure solution (ds+ps) creep models.

Fig. 13 shows that cavern convergence under cyclic loading conditions increases with depth, due to the higher temperatures and von Mises stresses associated with deeper locations. Under cyclic loading, the great-depth cavern exhibits the greatest convergence, reaching approximately 1.2% within the first 100 days. Also, the shallow cavern has a lower temperature, while the great-depth cavern experiences a higher temperature.

Fig. 13 illustrates that the percentage difference between the dislocation creep model (ds) and the dislocation–pressure solution creep model (ds+ps) increases at shallower depths, whereas this difference remains negligible at greater depths. This trend indicates that pressure solution creep has a stronger influence in colder, shallow regions of

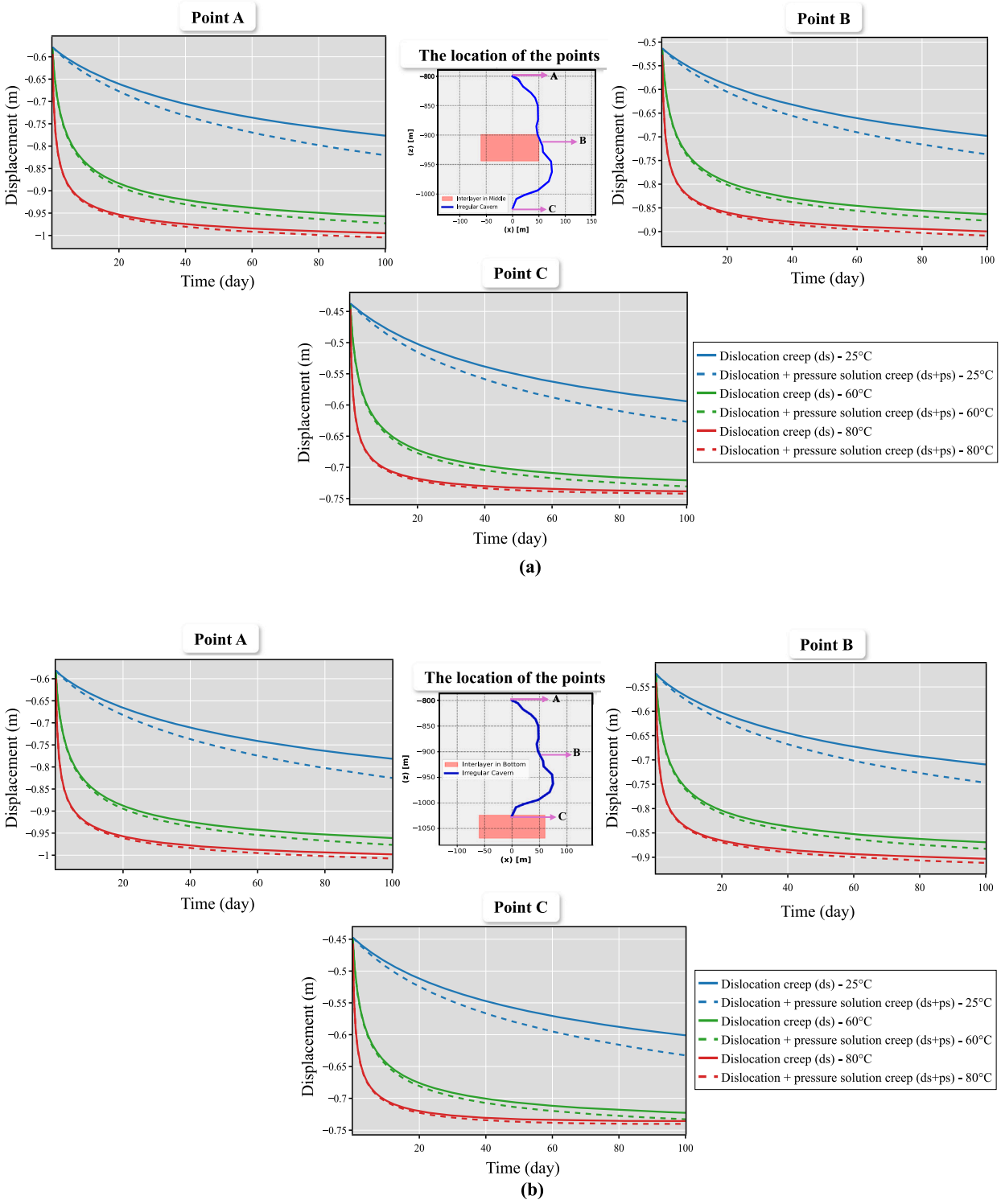

Fig. 10. Displacement at Points A, B, and C for the irregular cavern geometry with the Carnallite interlayer located (a) in the middle and (b) at the bottom of the cavern.

the cavern, while its contribution diminishes with increasing depth and temperature.

As illustrated in Fig. 8, the influence of pressure solution creep is more significant at lower von Mises stress (q) levels and lower temperatures. This is the case for the shallow cavern, where the von Mises stress is smaller compared to the cavern at greater depth. The figure further indicates that under lower temperature and low von Mises conditions, pressure solution creep plays a dominant role in the deformation process, whereas at greater depths characterized by higher temperatures and von Mises stresses, dislocation creep becomes the primary mechanism governing long-term deformation. Although these trends are qualitatively expected from the known dependence of creep on stress and temperature, this scenario quantitatively verifies that the implemented constitutive framework reproduces the correct transition between pressure solution and dislocation creep dominated regimes under realistic temperature gradients and lithostatic stress conditions.

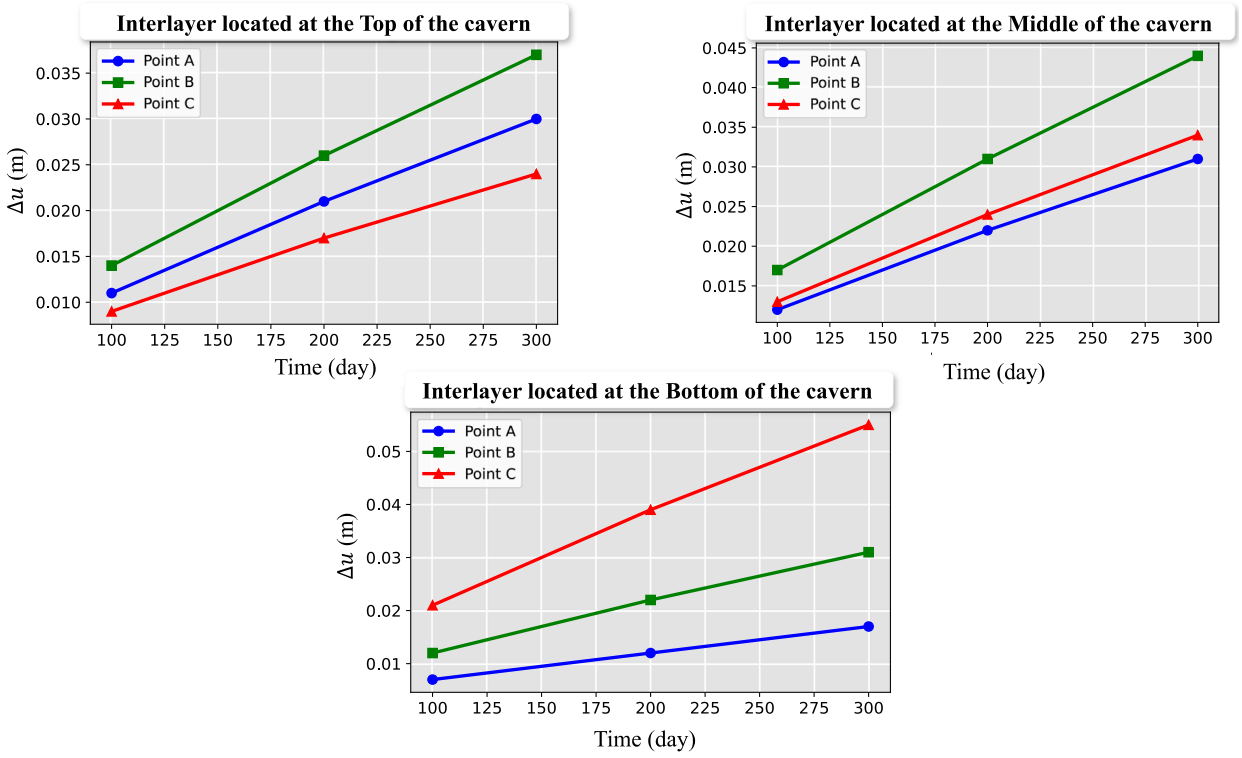

Fig. 11. Displacement difference $\Delta u = u_{ds+ps} - u_{ds}$ [m] between the dislocation-only and the dislocation plus pressure solution creep models at Points A, B, and C for the irregular cavern at 25 °C, based on new simulation results.

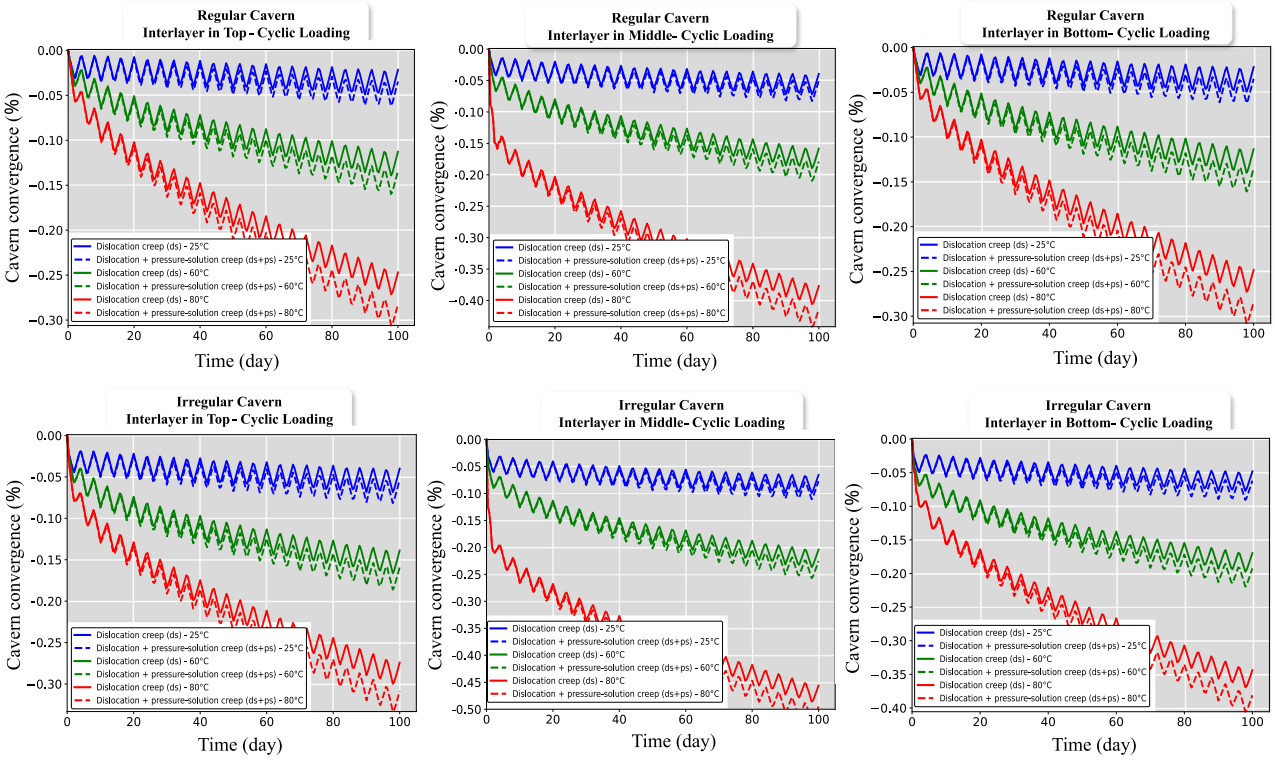

Fig. 12. Cavern convergence under cyclic loading condition for regular (top row) and irregular (bottom row) caverns geometries with interlayers positioned at the top, middle, and bottom. The plots compare the effects of temperature (25 °C, 60 °C, and 80 °C) and creep mechanisms (dislocation vs. dislocation + pressure solution) on the time-dependent convergence behavior over 100 days.

The test therefore confirms the robustness of the model when both pressure and temperature vary simultaneously, ensuring reliable prediction of depth-dependent deformation and stress distribution after extended operation (100 days and beyond).

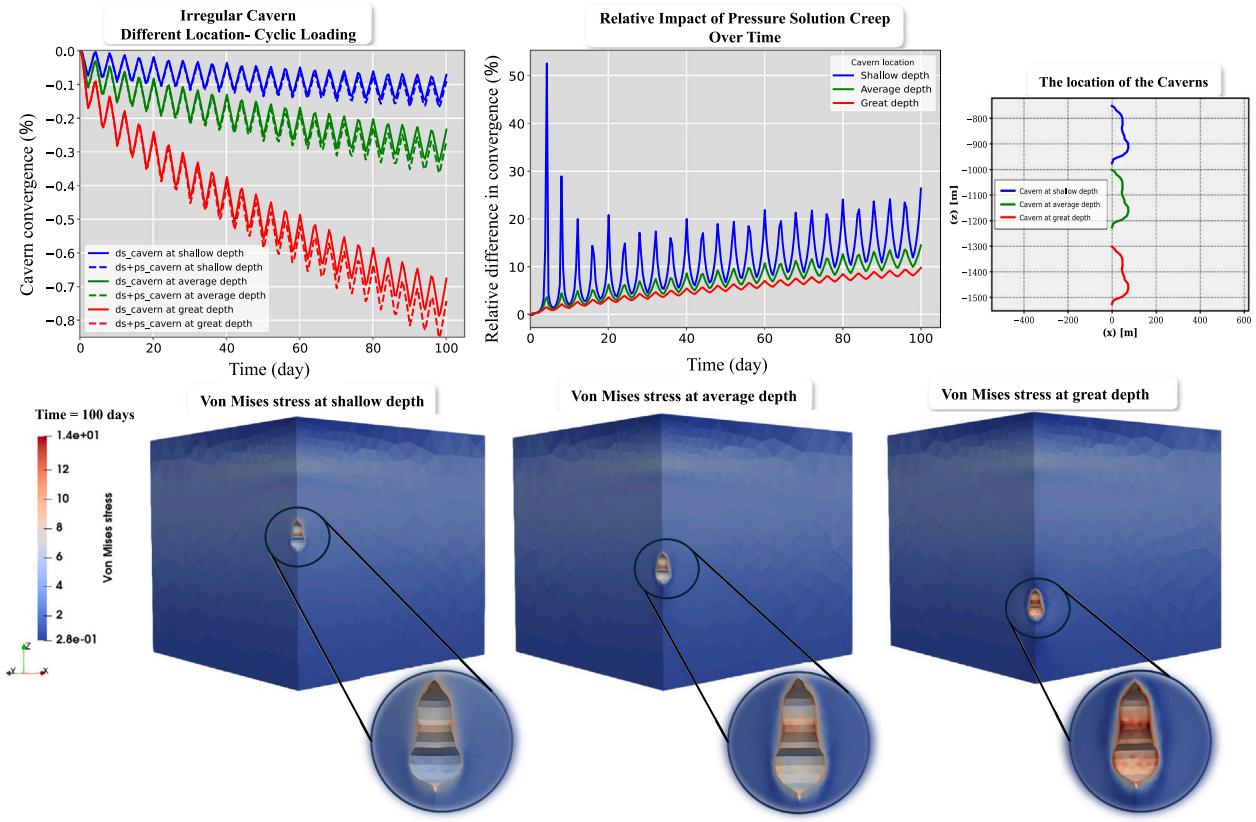

Fig. 13. Cavern convergence over time for irregular cavern geometries at different depths, using dislocation (ds) and dislocation plus pressure solution (ds+ps) creep models. Corresponding von Mises stress distributions q at $t = 100$ days for the three different cavern depths scenarios.

5. Conclusions

This study presents a comprehensive numerical investigation into the influence of pressure solution creep on the short- and long-term mechanical behavior of salt caverns used for underground hydrogen and energy storage. A creep formulation, which incorporates both the dislocation and pressure solution mechanisms, was developed and applied to a series of three-dimensional cavern models under geologically representative boundary and loading conditions. The simulations examined a variety of factors that affect the behavior of salt creep, including cavern geometry (regular vs. irregular), different cavern depth, interlayer positioning, and the effects of temperature gradient. The specific contribution of pressure solution creep was assessed by comparing models employing dislocation creep alone with those incorporating both mechanisms.

The key conclusions drawn from this investigation are listed below.

- The influence of pressure solution creep and the resulting displacement becomes increasingly significant over time, with only modest differences observed during the early stages, but substantial effects emerging after extended periods (200 and 300 days). Furthermore, the displacement is larger when an interlayer is present in the cavern shape, combined with an irregular cavern geometry and higher temperature conditions. In contrast, displacement is smaller under lower temperature (colder) conditions. This trend is also consistently observed in the cavern convergence.
- The comparison of creep model coefficients demonstrates that pressure solution creep dominates at lower temperatures. This trend is consistently supported by the numerical simulations, which show larger deformation differences in colder caverns when the pressure-solution mechanism is included.
- Convergence analysis reveals that the effects of pressure solution creep are consistently more pronounced at lower temperatures (25 °C) and in cases where interlayers are located in stress-intensified regions. For both regular and irregular cavern geometries, the inclusion of pressure solution creep mechanisms accelerates convergence, particularly under varying temperature conditions. While overall convergence tends to be larger in warmer caverns, the relative contribution of pressure solution creep is more significant in colder conditions.
- The analysis confirms that pressure solution creep is a dominant deformation mechanism in shallow or colder salt formations, whereas dislocation creep governs the behavior in deeper, high-temperature environments. At low temperatures ($T < 40\,°C$) and low von Mises stresses ($q \leq 3\,MPa$), pressure solution creep significantly exceeds dislocation creep, highlighting its critical role in long-term deformation under such conditions. In contrast, at high temperatures ($T \geq 80\,°C$), dislocation creep consistently dominates regardless of stress level, rendering the contribution of pressure solution creep negligible. Spatially, pressure solution creep is more active in regions far from the cavern wall, where both temperature and von Mises stress are relatively low, while dislocation creep is concentrated near the cavern walls, where higher stress and temperature prevail. These findings emphasize the necessity of incorporating pressure solution creep into predictive models for shallow or low-temperature underground storage caverns. Moreover, both creep mechanisms should be simultaneously considered in all analyses, as their combined interaction ensures more accurate predictions and minimizes modeling errors in the assessment of long-term cavern performance.

The present study delivers three specific quantitative insights that extend beyond established salt creep theory. First, the stress

–temperature thresholds at which each mechanism dominates are quantified at the cavern scale: pressure solution creep governs deformation across all operationally relevant stresses (1–20 MPa) at temperatures below 40 °C, whereas dislocation creep dominates at temperatures above 80 °C regardless of stress level. Second, the deformation error introduced by omitting pressure solution creep reaches up to 0.055 m at 300 days in shallow, cold formations, a magnitude with direct engineering significance for cavern design and safety assessment. Third, the spatial separation of mechanism dominance is resolved within the three-dimensional domain: dislocation creep concentrates near the cavern wall where stresses are highest, while pressure solution creep governs the far-field where both stress and temperature are low. These results translate laboratory-scale creep physics into operational-scale performance metrics and provide a quantitative basis for the design and long-term assessment of underground hydrogen storage systems.

CRediT authorship contribution statement

Mohammad Saeed Amini: Writing – original draft, Visualization, Validation, Software, Methodology, Investigation, Formal analysis, Conceptualization. **Hermínio T. Honório:** Writing – review & editing, Software, Methodology, Formal analysis, Conceptualization. **Cornelis Vuik:** Writing – review & editing, Supervision, Conceptualization. **Hadi Hajibeygi:** Writing – review & editing, Supervision, Methodology, Investigation, Funding acquisition, Formal analysis, Conceptualization.

Declaration of competing interest

The authors declare that they have no known competing financial interests or personal relationships that could have appeared to influence the work reported in this paper.

Acknowledgments

The authors acknowledge the funding of the European Union's Horizon Europe Research and Innovation programme under Marie Skłodowska-Curie for Doctoral Training Network (EU ITN) project "SHINE" with the Grant Agreement No. 101073271. The developments of this study have been made in an open-source "SafeInCave" simulator, which can be found in our Gitlab repository. Hadi Hajibeygi also acknowledges the supports of the Energi Simulation Chair in Subsurface Storage and Multiscale Modeling.

Appendix A. Strain rate derivatives

The consistent tangent operator $\mathbb{C}_T$ defined in Eq. (15) requires the explicit derivatives of each creep strain rate with respect to the stress tensor $\boldsymbol{\sigma}$. For dislocation creep, differentiating Eq. (5) via the chain rule gives:

$$\frac{\partial \dot{\epsilon}_{ij}^{\mathrm{ds}}}{\partial \sigma_{kl}} = A_{\mathrm{ds}} \exp\left(-\frac{Q_{\mathrm{ds}}}{RT}\right)\left[q^{n-1}\frac{\partial s_{ij}}{\partial \sigma_{kl}} + (n-1)\, q^{n-3}\, s_{ij}\, s_{mn}\frac{\partial s_{mn}}{\partial \sigma_{kl}}\right], \tag{19}$$

where A_{ds} [$\mathrm{Pa}^{-n}\,\mathrm{s}^{-1}$] is the dislocation creep pre-exponential coefficient, Q_{ds} is the corresponding activation energy, R is the universal gas constant, T is the absolute temperature, n is the stress exponent, q is the von Mises stress (see Eq. (8)), and s_{ij} are the components of the deviatoric stress tensor (see Eq. (7)). The derivative of the von Mises stress with respect to the stress tensor is obtained by differentiating $q = \sqrt{\frac{3}{2}\, s_{ij} s_{ji}}$, i.e.,

$$\frac{\partial q}{\partial \sigma_{kl}} = \frac{3}{2}\frac{s_{kl}}{q}. \tag{20}$$

For pressure solution creep, differentiating Eq. (6) gives

$$\frac{\partial \dot{\epsilon}_{ij}^{\mathrm{ps}}}{\partial \sigma_{kl}} = \frac{A_{\mathrm{ps}}}{T\, d^m}\exp\left(-\frac{Q_{\mathrm{ps}}}{RT}\right)\frac{\partial s_{ij}}{\partial \sigma_{kl}}, \tag{21}$$

where A_{ps} [$Pa^{-1}\, s^{-1}$] is the pressure solution pre-exponential coefficient, Q_{ds} is the pressure solution activation energy, d is the mean grain diameter, and m is the grain-size exponent. Note that Eq. (21) is *stress-independent* because $\dot{\boldsymbol{\epsilon}}_{ps}$ is linear in $\mathbf{s}$; nevertheless it must be included in $\mathbb{G}_{\mathrm{ie}}$ at every Newton–Raphson iteration (see the convergence remark below).

The derivative of the deviatoric stress tensor, shared by both Eqs. (19) and (21), follows directly from Eq. (7), i.e.,

$$\frac{\partial s_{ij}}{\partial \sigma_{kl}} = \tfrac{1}{2}\left(\delta_{ik}\delta_{jl} + \delta_{il}\delta_{jk}\right) - \tfrac{1}{3}\,\delta_{ij}\,\delta_{kl}, \tag{22}$$

where δ_{ij} is the Kronecker delta and indices i, j, k, l, m, n range over $\{1, 2, 3\}$ with repeated indices implying Einstein summation.

The complete tangent operator is assembled as $\mathbb{G}_{\mathrm{ie}} = \partial\dot{\boldsymbol{\epsilon}}_{\mathrm{ds}}/\partial\boldsymbol{\sigma} + \partial\dot{\boldsymbol{\epsilon}}_{\mathrm{ps}}/\partial\boldsymbol{\sigma}$ from Eqs. (19)–(22). It is worth to be mentioned that although the pressure solution contribution, i.e., Eq. (21), is stress-independent, it must be included in the Jacobian matrix $\mathbb{G}_{\mathrm{ie}}$ at every Newton–Raphson iteration to preserve the quadratic convergence of the nonlinear solver.

Appendix B. Supplementary data

Supplementary material related to this article can be found online at https://doi.org/10.1016/j.ijrmms.2026.106555.

Data availability

the codes and data are open source.

References

1. Jarbratt G, Spare E, Jautelat S, Linder M. *Enabling renewable energy with battery energy storage systems*. McKinsey & Company; 2023.
2. Polidoro Franco. Safety aspects related to the underground hydrogen storage. *Hydrog Knowl Cent*. 2023.
3. Krevor Samuel, De Coninck Heleen, Gasda Sarah E, Ghaleigh Navraj Singh, de Gooyert Vincent, Hajibeygi Hadi, Juanes Ruben, Neufeld Jerome, Roberts Jennifer J, Swennenhuis Floris. Subsurface carbon dioxide and hydrogen storage for a sustainable energy future. *Nat Rev Earth Environ*. 2023;4(2):102–118.
4. Miocic Johannes, Heinemann Niklas, Edlmann Katriona, Scafidi Jonathan, Molaei Fatemeh, Alcalde Juan. Underground hydrogen storage: a review. *Geol Soc Lond Spec Publ*. 2023;528.
5. Małachowska A, Łukasik N, Mioduska J, Gebicki J. Hydrogen storage in geological formations—The potential of salt caverns. *Energies*. 2022;15:5038.
6. Lankof Leszek, Tarkowski Radosław. Assessment of the potential for underground hydrogen storage in bedded salt formation. *Int J Hydrog Energy*. 2020;45(38):19479–19492.
7. Tarkowski Radosław, Czapowski Grzegorz. Salt domes in Poland–Potential sites for hydrogen storage in caverns. *Int J Hydrog Energy*. 2018;43(46):21414–21427.
8. Liu Wei, Zhang Zhixin, Chen Jie, Jiang Deyi, Wu Fei, Fan Jinyang, Li Yinping. Feasibility evaluation of large-scale underground hydrogen storage in bedded salt rocks of China: A case study in jiangsu province. *Energy*. 2020;198:117348.
9. Oni Babalola Aisosa, Bade Shree Om, Sanni Samuel Eshorame, Orodu Oyinkepreye David. Underground hydrogen storage in salt caverns: recent advances, modeling approaches, barriers, and future outlook. *J Energy Storage*. 2025;107:114951.
10. Hui Shasha, Yin Shunde, Pang Xiongqi, Chen Zhuoheng, Shi Kanyuan. Potential of salt caverns for hydrogen storage in southern Ontario, Canada. *Mining*. 2023;3(3):399–408.
11. Ozarslan Ahmet. Large-scale hydrogen energy storage in salt caverns. *Int J Hydrog Energy*. 2012;37(19):14265–14277.
12. Huang Jingyu, Yin Shunde. Optimization of the design of underground hydrogen storage in salt caverns in Southern Ontario, Canada. *Mining*. 2025;5(1):9.
13. Liu Zhongzhong, Liu Yuxuan. Research on the stability of salt cavern hydrogen storage and natural gas storage under long-term storage conditions. *Processes*. 2024;12(10).
14. Chang Kyung Won, Ross Tonya SA. Cyclic loading-unloading impacts on salt cavern stability: Implication for underground hydrogen storage. In: *ARMA US rock mechanics/geomechanics symposium*. ARMA; 2024:D042S057R001.
15. Grgic D, Al Sahyouni F, Golfier F, Moumni M, Schoumacker L. Evolution of gas permeability of rock salt under different loading conditions and implications on the underground hydrogen storage in salt caverns. *Rock Mech Rock Eng*. 2022:1–24.

16. Honório Hermínio T, Houben Maartje, Bisdom Kevin, van der Linden Arjan, de Borst Karin, Sluys Lambertus J, Hajibeygi Hadi. A multi-step calibration strategy for reliable parameter determination of salt rock mechanics constitutive models. *Int J Rock Mech Min Sci*. 2024;183:105922.
17. Vitali Osvaldo PM. Geomechanics behavior of salt caverns following depressurization and backfilling. *Int J Geomech*. 2025;25(4):04025039.
18. Passaris Evan. In situ geomechanical investigations used in the design of hydrogen storage caverns. In: *Proceedings of the 9th international congress on environmental geotechnics*. ARGO-E; 2023.
19. Habibi Rahim. An investigation into design concepts, design methods and stability criteria of salt caverns. *Oil Gas Sci Technology–Revue D'IFP Energies Nouv*. 2019;74:14.
20. Zhang Huabin, Li Quanen, Yue Xianru, Ba Jinhong, Ding Shuanglong. Study on the deformation and failure laws of surrounding rock under reduced roof thickness in salt cavern gas storage. *Sci Rep*. 2024;14(1):22529.
21. Tian Deyan, Khaledi Kavan, Jalali Mohammadreza, Amann Florian. Long-term cyclic thermo-mechanical behavior of vertical and horizontal salt caverns for hydrogen storage. 2024 Available At SSRN.
22. Liu Jianjun, Xiao Qiang. The influence of operation pressure on the long-term stability of salt-cavern gas storage. *Adv Mech Eng*. 2014;6:537679.
23. Ramesh Kumar Kishan, Makhmutov Artur, Spiers Christopher J, Hajibeygi Hadi. Geomechanical simulation of energy storage in salt formations. *Sci Rep*. 2021;11(1):19640.
24. Habibi Rahim, Moomivand Hassan, Ahmadi Mortez, Asgari Amin. Stability analysis of complex behavior of salt cavern subjected to cyclic loading by laboratory measurement and numerical modeling using LOCAS. *Environ Earth Sci*. 2021;80:317.
25. berest Pierre, Gharbi Hakim, Brouard Benoit, Brückner Dieter, DeVries Kerry, Hévin Grégoire, Hofer Gerd, Spiers Christopher, Urai Janos. Very slow creep tests on salt samples. *Rock Mech Rock Eng*. 2019;52:2917–2934.
26. Tarifard Abolfazl, Török Ákos, Görög Péter. Review of the creep constitutive models for rocks and the application of creep analysis in geomechanics. *Rock Mech Rock Eng*. 2024;57(10):7727–7757.
27. Li Zongze. *Study on creep fatigue mechanical characteristics and constitutive model of salt rock* [Ph.D. thesis]. INSA de Lyon; Chongqing university; 2023.
28. Zhang Qiang, Song Zhanping, Wang Junbao, Zhang Yuwei, Wang Tong. Creep properties and constitutive model of salt rock. *Adv Civ Eng*. 2021;2021(1):8867673.
29. Carter Neville L, Hansen Francis D. Creep of rocksalt. *Tectonophysics*. 1983;92(4):275–333.
30. Carter NL, Horseman ST, Russell JE, Handin J. Rheology of rocksalt. *J Struct Geol*. 1993;15(9–10):1257–1271.
31. Rutter EH. Pressure solution in nature, theory and experiment. *J Geol Soc*. 1983;140(5):725–740.
32. Urai Janos L, Spiers Christopher J, Zwart Hendrik J, Lister Gordon S. Weakening of rock salt by water during long-term creep. *Nature*. 1986;324(6097):554–557.
33. Berest P, Brouard B. A tentative classification of salts according to their creep properties. In: *Meeting new orleans, louisiana, USA*. 1998:19–22.
34. Bérest Pierre, Blum Pierre Antoine, Charpentier Jean Pierre, Gharbi Hakim, Valès Frédéric. Very slow creep tests on rock samples. *Int J Rock Mech Min Sci*. 2005;42(4):569–576.
35. Van Oosterhout BGA, Hangx SJT, Spiers CJ. A threshold stress for pressure solution creep in rock salt: Model predictions vs. observations. In: *The mechanical behavior of salt x*. CRC Press; 2022:57–67.
36. Speirs DCD, Bere A, Roberts D. Geomechanical modelling of salt caverns under operational loading from hydrogen storage. In: *ARMA/DGS/sEG international geomechanics symposium*. ARMA; 2022:ARMA–IGS.
37. Hunfeld Luuk, Breunese Jaap, Wassing Brecht. The influence of a threshold stress for pressure solution creep on cavern convergence and subsidence behavior–an FEM study. In: *The mechanical behavior of salt x*. CRC Press; 2022:577–589.
38. Gratier Jean-Pierre, Dysthe Dag K, Renard François. The role of pressure solution creep in the ductility of the earth's upper crust. *Adv Geophys*. 2013;54:47–179.
39. Bérest P, Béraud JF, Gharbi H, Brouard B, DeVries K. A very slow creep test on an Avery Island salt sample. *Rock Mech Rock Eng*. 2015;48:2591–2602.
40. Cristescu ND. Time effects in rock mechanics. Citeseer; 2009. In: Society for experimental mechanics (SEM)–annual conference and exposition on experimental and applied mechanics; vol. 2.
41. Urai JL. Deformation mechanisms operating in naturally deformed halite rocks as deduced from microstructural investigation. *Geol Mijnb*. 1987;66:165–176.
42. Spiers CJ, Schutjens PMTM, Brzesowsky RH, Peach CJ, Liezenberg JL, Zwart HJ. Experimental determination of constitutive parameters governing creep of rocksalt by pressure solution. *Geol Soc Lond Spec Publ*. 1990;54(1):215–227.
43. Spiers Chiristopher J, Carter Neville L. Microphysics of rocksalt flow in nature. *Ser Rock Soil Mech*. 1998:115–128.
44. Bérest Pierre. Cases, causes and classifications of craters above salt caverns. *Int J Rock Mech Min Sci*. 2017;100:318–329.
45. Kumar Kishan Ramesh, Hajibeygi Hadi. Influence of pressure solution and evaporate heterogeneity on the geo-mechanical behavior of salt caverns. In: *The mechanical behavior of salt x*. CRC Press; 2022:407–420.
46. Herchen K, Popp T, Düsterloh U, Lux KH, Salzer K, Lüdeling C, Günther RM, Rölke C, Minkley W, Hampel A, et al. WEIMOS: Laboratory investigations of damage reduction and creep at small deviatoric stresses in rock salt. In: *Proceedings of the conference on mechanical behavior of salt, saltMech IX, hannover, Germany, September*. 2018:12–18.
47. Kumar Kishan Ramesh, Honorio Herminio, Chandra Debanjan, Lesueur Martin, Hajibeygi Hadi. Comprehensive review of geomechanics of underground hydrogen storage in depleted reservoirs and salt caverns. *J Energy Storage*. 2023;73:108912.
48. Honório Hermínio T, Hajibeygi Hadi. Three-dimensional multi-physics simulation and sensitivity analysis of cyclic energy storage in salt caverns. *Int J Hydrog Energy*. 2024;94:1389–1405.
49. Zhou Y, Li S, Xu T, Liu W. Numerical analysis of salt cavern deformation under coupled dislocation and pressure solution creep mechanisms. *Comput Geotech*. 2021;139:104347.
50. Wang X, Liu J, Zhao J, Jiang Q. Creep behavior of bedded salt rock considering pressure solution mechanism. *Int J Rock Mech Min Sci*. 2014;72:207–217.
51. Rothfuchs T, Heim S. Simulation of long-term creep in rock salt considering pressure solution mechanisms. *Eng Geol*. 1998;50(3–4):255–266.
52. Munson DE, Dawson PR. A transient creep model for salt during stress loading and unloading. *Int J Rock Mech Min Sci Geomech Abstr*. 1982;19(5):259–272.
53. Munson DE, Dawson PR. Salt constitutive modeling using mechanism maps. *J Geophys Res*. 1984;89:6923–6934.
54. Liu W, Li Y, Zhang Y, Yang C. Stability analysis of complex behavior of gas storage salt caverns subjected to cyclic loading. *Arab J Geosci*. 2021;14:1–15.
55. Yang Fan, Fan Jinyang, Yang Zhenyu, Liu Wei, Chen Jie. Plasticity analysis and constitutive model of salt rock under different loading speeds. *J Energy Storage*. 2023;67:107583.
56. Wang Herbert. Princeton University Press; 2000. Theory of linear poroelasticity with applications to geomechanics and hydrogeology; vol. 2.
57. Khan Akhtar S, Wang Xinwei. *Strain measurements and stress analysis*. Upper Saddle River, New Jersey: Prentice Hall; 2001.
58. Visser William. *High strain rate deformation mechanisms of body centered cubic material subjected to impact loading*. University of Rhode Island; 2017.
59. Manjoine MJ. Multiaxial stress and fracture. In: *Engineering fundamentals and environmental effects*. Elsevier; 1971:265–309.
60. Lu Renchao. *Hydro-mechanical-chemical coupled processes in fractured porous media: pressure solution creep* [Ph.D. thesis]. Technische Universität Dresden; 2020.
61. Ingraham Mathew Duffy, Broome Scott Thomas, Bauer Stephen J, Barrow Perry Carl, Flint Gregory Mark. Behavior of salt from the bayou choctaw salt dome. In: *ARMA US rock mechanics/geomechanics symposium*. ARMA; 2015:ARMA–2015.
62. Muhammad Nawaz, et al. *Deformation and transport processes in salt rocks: an experimental study exploring effects of pressure and stress relaxation* [Ph.D. thesis]. UU Dept. of Earth Sciences; 2015.
63. Muhammad N, de Bresser JHP, Peach CJ, Spiers CJ. Creep behaviour of bischofite, carnallite and mixed bischofite–carnallite–halite salt rock at in situ conditions. In: *The mechanical behavior of salt x*. CRC Press; 2022.
64. Luangthip A, Wilalak N, Thongprapha T, Fuenkajorn K. Effects of carnallite content on mechanical properties of Maha Sarakham rock salt. *Arab J Geosci*. 2017;10:149.
65. Logg Anders, Mardal Kent-Andre, Wells Garth. Springer Science & Business Media; 2012. Automated solution of differential equations by the finite element method: The FEniCS book; vol. 84.
66. Alnæs Martin, Blechta Jan, Hake Johan, Johansson August, Kehlet Benjamin, Logg Anders, Richardson Chris, Ring Johannes, Rognes Marie E, Wells Garth N. The FEniCS project version 1.5. *Arch Numer Softw*. 2015;3(100).
67. Geuzaine Christophe, Remacle Jean-François. Gmsh: A 3-D finite element mesh generator with built-in pre-and post-processing facilities. *Internat J Numer Methods Engrg*. 2009;79(11):1309–1331.